Surface Coating Mediated Swelling and Fracture of Silicon Nanowires during Lithiation

Georgiana Sandu,[†,⊥] Laurence Brassart,[‡,⊥] Jean-François Gohy,[§] Thomas Pardoen,[‡] Sorin Melinte,[†] and Alexandru Vlad[†,*]

[†]Institute of Information and Communication Technologies, Electronics and Applied Mathematics, [‡]Institute of Mechanics, Materials, and Civil Engineering, and [§]Institute of Condensed Matter and Nanosciences, Université Catholique de Louvain, 1348 Louvain-la-Neuve, Belgium. [⊥]G. Sandu and L. Brassart contributed equally.

ABSTRACT Surface passivation of silicon anodes is an appealing design strategy for the development of reliable, high-capacity lithium-ion batteries. However, the structural stability of the coating layer and its influence on the lithiation process remain largely unclear. Herein, we show that surface coating mediates the swelling dynamics and the fracture pattern during initial lithiation of crystalline silicon nanopillars. We choose conformally nickel coated silicon architectures as a model system. Experimental findings are interpreted based on a chemomechanical model. Markedly different swelling and fracture regimes have been identified, depending on the coating thickness and silicon nanopillar diameter. Nanopillars with relatively thin coating display anisotropic swelling similar to pristine nanopillars, but with different preferred fracture sites. As the coating thickness increases, the mechanisms become isotropic, with one randomly oriented longitudinal crack that unzips the core–shell structure. The morphology of cracked pillars resembles that of a thin-film electrode on a substrate, which is more amenable to cyclic lithiation without fracture. The knowledge provided here helps clarify the cycling results of coated nanosilicon electrodes and further suggests design rules for better performance electrodes through proper control of the lithiation and fracture.

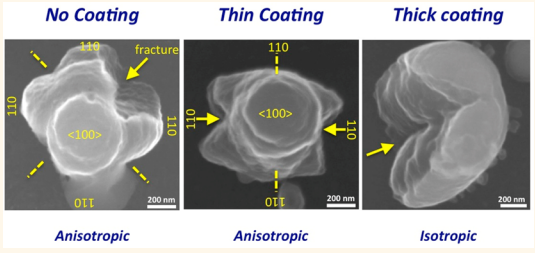

KEYWORDS: lithium insertion · silicon anode · metal coating · semiconductor nanowires · core–shell nanostructures · isotropy

Lithium-ion batteries (LIBs) constitute an enabling technology for size- and shape-sensitive applications such as portable electronics and electric vehicles.[1] One promising direction for increasing the energy density is to replace conventional negative intercalation electrodes by lithium alloys. Silicon is a particularly attractive candidate given its enormous specific capacity and low working potential.[2] However, the alloying reaction of Li with Si involves huge volume change, inducing large internal stresses when the expansion is constrained or nonhomogeneous.[3] Stresses in turn lead to mechanical degradation, loss of the electrical contact, and, ultimately, rapid capacity fade. Moreover, an unstable solid-electrolyte interphase (SEI) is continuously generated, further diminishing the Coulombic efficiency.[4] These failure mechanisms can be partially mitigated in engineered Si anodes, such as nanostructures,[5,6] composites, and complex architectures,[7–10] which accommodate the volume change without damage. Effective passivation of the electrode surface can be achieved using binders[11,12] and electrolyte additives.[13] Despite this recent progress, sustaining long cycle life at deep lithiation levels remains troublesome.

Recent studies showed that functional surface coatings comprising metals, carbon, or oxides can positively impact the cycling stability of the Si anode.[9,10,14–23] These improvements have been attributed to several factors. First, a surface coating prevents the direct contact with the electrolyte and, thus, controls the SEI formation. Second, surface coating can act as a mechanical constraining layer by buffering the volume change, preventing electrode pulverization. Furthermore, electronically conducting coatings (such as metal and carbon) improve the current collection efficiency, thus enhancing the redox reaction kinetics at the electrode. Finally, a surface coating can also

* Address correspondence to alexandru.vlad@uclouvain.be.

Received for review July 1, 2014 and accepted August 18, 2014.

Published online August 18, 2014
10.1021/nn503564r

prevent detrimental electrochemical welding between active material particles.[24−26]

A key feature of coated Si structures is their mechanical stability when deformed by the constrained expansion of the core. If the coating layer cracks, much of the listed benefits are simply lost. The electrical conductivity can be severely affected by the generated discontinuities, whereas the direct exposure of a fresh silicon surface to the electrolyte inevitably results in new SEI formation. Eventually, cracks initiated in the surface layer may propagate into the lithiated silicon, further amplifying the degradation. Despite the general consideration that surface coating enables sustained cycling, single-particle *in situ* studies have actually revealed irreversible and dramatic damages to the coating, not fully corroborating the larger scale electrochemical cycling experiments.[20,21,23] Furthermore, while carbon coatings have been generally considered as beneficial for cycling stability and charge collection efficiency, carbon becomes brittle when lithiated,[27] delaminates,[28] and undergoes dramatic irreversible damage.[21] Finally, cracking of metallic coatings during lithiation was also reported.[20] Whereas hollow nanostructures have been shown to maintain structural integrity by directing the volume expansion toward the interior,[9,17,28,29] scalability of the fabrication processes, low mass loading, and progressive SEI accumulation in the internal void spaces limit their widespread implementation. Understanding and controlling the lithiation dynamics as well as the swelling and fracture behavior in coated Si structures are thus of primary interest toward real-life battery applications.

Herein, we selected nickel-coated silicon nanopillars as a model system for analyzing the swelling and fracture behavior during the initial lithiation. Nickel was selected because of its high electron conductivity and good adherence to silicon. Furthermore, nickel hinders excessive SEI formation, has a low reactivity with lithium, yet allows a lithium flux.[6,9,16,30−33] We report markedly different swelling and fracture patterns depending on the coating thickness and the silicon nanopillar diameter. Nanopillars with relatively thin coating display anisotropic swelling similar to that observed in the case of pristine nanopillars, but with different preferred fracture sites. As the coating thickness increases, swelling and fracture patterns undergo an anisotropic to isotropic transition, with a single randomly oriented longitudinal crack. We carry out a numerical chemomechanical analysis suggesting that the transition from anisotropic to isotropic behavior follows from the mechanically altered lithiation kinetics. While fracture in plain, coated silicon nanostructures seems inevitable, our results suggest that the fracture pattern could be tailored through an appropriate choice of the coating thickness and morphology.

CORE−SHELL SI NANOPILLAR DESIGN AND TESTING

The crystalline silicon nanopillars of ⟨100⟩ axial crystal orientation have been fabricated using combined nanosphere lithography and metal-assisted chemical etching protocols as previously reported,[10] enabling thus precise crystallographic orientation mapping and visualization. An electroless deposition procedure was selected for the conformal coating of the nanopillars with Ni. This procedure allows the growth of a Ni layer with a uniform thickness along the radial and axial directions (Figure 1a and b) and a precise morphology control (see Supporting Information for details). Contrarily to commonly used physical vapor deposition techniques[9,14,20,21] which are directional and cannot coat complex geometries and configurations, the adopted procedure is scalable and could be applied as well to other silicon morphologies including particles and powders. In order to investigate the impact of the structure dimensions, we processed Si nanopillars with different nominal diameters (170, 330, and 480 nm) and varying coating thicknesses (40, 80, and 120 nm) (Figure 1a; see also Supporting Information Figure S1 for details on the morphology and microstructure of the Ni-coated Si nanopillars). For simplicity, the composite structures are referred to as $Si_{2A}@Ni_h$, where subscripts *A* and *h* stand for the Si core radius and Ni shell thickness, respectively. The composite structure is considered isotropic and at equilibrium before lithiation.

The lithiation of coated Si nanopillars follows a documented *ex situ* experimental protocol (see Supporting Information for details).[33,34] In short, the setup consists in a half-cell with the composite nanopillars supported by the Si substrate as working electrode and a Li-metal foil as reference and counter electrode (Figure 1c). The cell voltage was slowly ramped down to 10 mV *vs* Li/Li^+ and held at this potential for at least 6 h (Figure 1d). Such conditions ensure a deep lithiation of pristine nanopillars, as revealed by post-mortem selective removal of the lithiated Si phase (see also Supporting Information). However, coated structures displayed a markedly different behavior during lithiation. In particular, thick Ni coatings were found to severely slow down the initial lithiation of the nanopillars (see hereafter), requiring a longer lithiation time (more than 12 h). Eventually, this led to fracture and pulverization of the underlying silicon substrate, resulting in the loss of electrical contact with the bottom current collector (circuit C1 in Figure 1c). To avoid this and to force lithiation, the electrical contact was established through the Ni layer covering the substrate top surface and the Si nanopillars (circuit C2 in Figure 1c). Finally, it is worth noting that due to severe substrate disintegration, subsequent delithiation and further cycling was not possible.

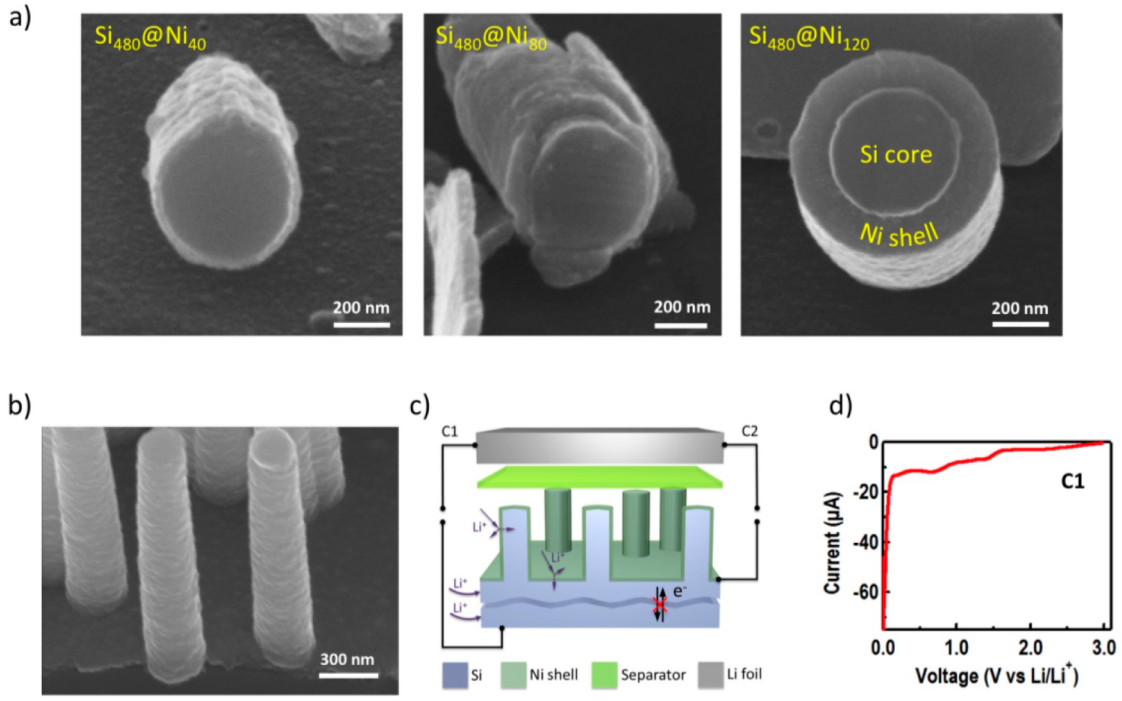

Figure 1. Experimental design. (a) Cross-section SEM views of the conformal Ni shell with different thicknesses deposited around the circular silicon core nanopillar. (b) SEM side view of conformally Ni wrapped silicon nanopillars. (c) Schematic of the lithiation setup. Two circuit configurations have been used depending on the metal shell thickness: C1 for uncoated Si or thin Ni deposits and C2 for thick Ni coatings. (d) Typical current *vs* voltage profile during electrochemical lithiation experiments.

LITHIATION RESULTS

Figure 2a shows representative morphologies of $Si_{480}@Ni_0$ after lithiation. Note that the pristine Si nanopillars already have a surface coating made of native SiO_2, of approximately 2 nm thickness. Consistent with previous reports, bare silicon nanopillars display anisotropic swelling with preferentially faster expansion on the {110} planes.[33−36] The anisotropic swelling of crystalline Si during solid-state amorphization results from the different reaction kinetics on the {110}, {100}, and {111} crystallographic planes.[37,38] The lithiated nanopillars typically display one or two axial cracks on the surface of {100} lateral planes, consistent with previous reports (Figure 2a, fracture site statistics).

Coated nanopillars exhibit a markedly different behavior. Distinct swelling behavior and accompanying fracture regimes have been identified in nanopillars with respectively "thin" ($Si_{480}@Ni_{40}$ and $Si_{480}@Ni_{80}$ display similar patterns; see Supporting Information, Figure S2) and "thick" ($Si_{480}@Ni_{120}$) coatings. For thin coatings, the lithiation-induced cracks are now located on the surface of {110} lateral planes, as evidenced by scanning electron microscopy (SEM) images and the statistical analysis presented in Figure 2b. Cracks nucleate in the Ni shell and propagate into the Li_xSi as the lithiation proceeds (Supporting Information, Figure S9). Several cracks can be accommodated within the same structure. Nanopillars with up to three cracks have been observed, while only a single crack per nanopillar was usually identified in the uncoated structures. Whereas the lithiation-induced swelling anisotropy for $Si_{480}@Ni_{40}$ and $Si_{480}@Ni_{80}$ configurations is less obvious than in $Si_{480}@Ni_0$, the existence of clear preferential fracture sites unambiguously suggests that the underlying morphology evolution retains its anisotropic swelling character. Furthermore, cracked nanopillars exhibit asymmetric morphology evolution, indicative of preferential lithiation through the cracks (see also Supporting Information, Figure S9). In contrast, the remaining undamaged {110} planes do not exhibit large deformation, indicating a lower degree of lithiation.

Further increase of the coating thickness induces yet another swelling and fracture scenario (Figure 2c). The lithiated $Si_{480}@Ni_{120}$ nanopillars display only one fracture site per nanopillar and, remarkably, the crack shows no preferential crystallographic orientation (Figure 2c, fracture site statistics). The crack propagates radially through the nanopillar section and may ultimately split the latter into two roughly symmetric half-cylinders. Noticeably, the lithiated silicon half-core is protruding from inside, whereas the Ni half-shells roughly maintain their original shape. However, the observed radial expansion varies for different nanopillars (Figure 2c, middle panel). Assuming a uniform expansion along the axis and neglecting any axial expansion (see below), this observation suggests that the extent of lithiation varies from nanopillar to nanopillar. This was further confirmed by selective methanol etching of the lithiated Si phase (see the Supporting

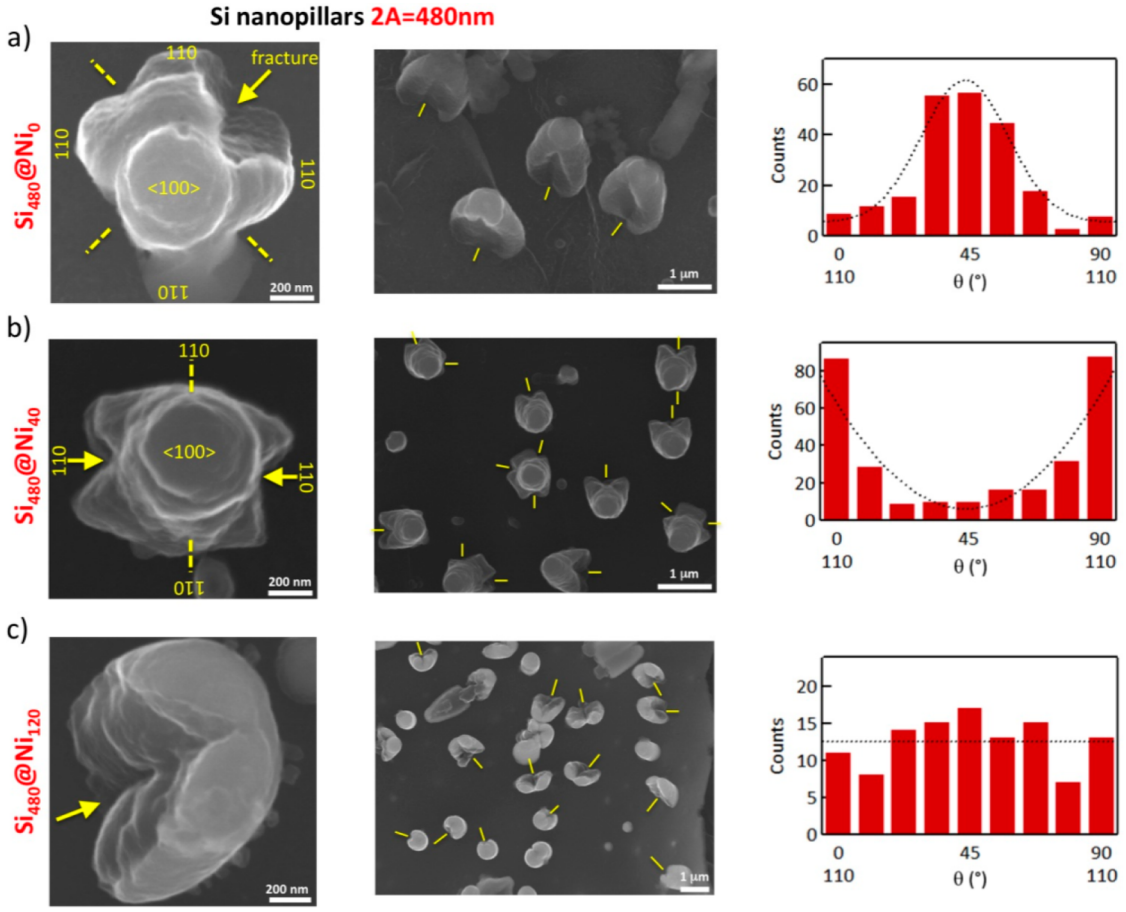

Figure 2. Nickel shell mediated swelling and fracture. High- and low-magnification SEM micrographs of lithiated silicon pillars as well as statistical analysis of the cracking sites for pristine (row a), 40 nm (row b), and 120 nm (row c) thick Ni-coated silicon nanopillars. The angular location of cracking sites (θ) is measured with respect to one quadrant delimited by the ⟨110⟩ directions. The dashed lines indicate the preferred location of the cracks, while the arrows point to developed cracks. The swelling and the cracking behaviors of core−shell structures markedly vary with the coating thickness. The dashed lines in the fracture histograms are fits of experimental data and intended as guidelines to the eye.

Information), which revealed a distribution in the sizes of the remaining c-Si cores. However, the amount of absorbed Li in each nanopillar could not be precisely quantified, so that the above analysis remains qualitative. Also, some nanopillars appear not to be affected at all. This is noteworthy given that these experiments were performed for 24 h or more using the circuit configuration C2 (to ensure reliable electrical contact, Figure 1c). In contrast, under similar lithiation conditions, pristine as well as thin Ni-coated nanopillars were systematically found to be fully lithiated. Various degrees of radial crack advancement among the nanopillars can be visualized as well. This suggests that lithiation may be slowed down even after the onset of fracture of the Ni shell. However, these cracks were always found to run all the way down the nanopillars. Finally, within the SEM resolution limit, neither apparent expansion in the axial direction nor transverse cracks could be detected in any of the studied configurations, in agreement with previous literature reports.[39]

We have performed a similar analysis on nanopillars with smaller initial Si diameter (see Supporting Information, Figures S3 and S4). As expected, the $Si_{330}@Ni_0$ and $Si_{170}@Ni_0$ configurations display the preferential swelling anisotropy normal to the {110} planes. However, the anisotropic deformation of small-diameter nanopillars is less pronounced, as previously reported.[34,40,41] For instance, whereas cross-shaped morphologies can be clearly visualized for the pristine diameters larger than 350 nm, rectangular shapes are barely distinguished for diameters below 170 nm (see Supporting Information, Figure S4a). On the other hand, coated $Si_{330}@Ni_{40}$, $Si_{330}@Ni_{90}$, and $Si_{170}@Ni_{40}$ nanopillars overall display isotropic cracking and swelling patterns. Only one fracture site with no apparent preferred orientation is observed, similar to the previously detailed $Si_{480}@Ni_{120}$ configuration. However, in contrast to the $Si_{480}@Ni_{120}$ case, a larger fraction of small-diameter nanopillars was found to be lithiated and cracked.

MODELING AND ANALYSIS

The broad spectrum in the swelling and fracture behavior suggests a complex interplay between various chemomechanical processes, depending on the

characteristic dimensions of the system of interest. The initial lithiation of crystalline silicon at room temperature results in the formation of an amorphous Li_xSi phase ($x \approx 3.75$)[2] that progresses toward the interior of the nanopillars.[39,42] Anisotropic growth of the lithiated phase is explained by the orientation-dependent mobility of the reaction front.[37−39,43] Lithiation also requires the transport of Li through the Ni coating and the lithiated phase, up to the reaction front. As lithiation proceeds, stresses are generated as a result of the heterogeneous swelling and constraining action of the Ni layer. Stresses may in turn significantly impact the various chemical processes. In the following, we rely on a chemomechanical analysis to gain more insight into the relevant factors governing the observed swelling and fracture regimes. We particularly discuss (i) Li transport through the Ni coating, (ii) the buffering effect of the Ni layer, and (iii) the impact of stress on the lithiation kinetics.

Diffusion of Li through Ni metal films is often considered as improbable because no Li−Ni alloys are known at room temperature. However, some analyses have shown that Li can freely move through inert metallic films (Cu or Ni), which are efficiently used as an ion-selection membrane or for surface passivation.[9,16,36] Although we could not determine the precise value, Li diffusivity is estimated to fall in the range 10^{-9}−10^{-11} cm^2/s. The lower bound for Li diffusivity in Ni is therefore still orders of magnitude higher than that of Li through Li_xSi, estimated at around 10^{-12}−10^{-14} cm^2/s. In turn, diffusion of Li through lithiated silicon is very fast compared to the lithiation reaction kinetics.[37] Overall, the entire process is reaction-limited, rather than diffusion-limited. On the basis of these considerations, Li diffusion through Ni is thus considered as having a negligible impact on the observed swelling and fracture patterns.

To investigate the effect of the Ni layer on the morphological evolution and stress development during lithiation, we implemented a 2D continuum chemomechanical model into the Finite Elements software Abaqus (see Supporting Information for a complete description of the model). Silicon is modeled as an elastoplastic material with material properties varying with Li concentration. Nickel is modeled as an elastoplastic, strain-hardening material with properties independent of Li content. Swelling of the lithiated phase is simulated by applying an (isotropic) eigenstrain proportional to the local Li concentration. The velocity of the reaction front is prescribed and varies with the crystallographic orientation. In ⟨100⟩ axially oriented silicon nanopillars, this implies faster lithiation in the direction perpendicular to the {110} crystallographic planes (Supporting Information, Figure S5). Simulation of the lithiation of uncoated nanopillars (Supporting Information, Figures S5 and S6) predicts a cross-shaped morphology in good agreement with experimental observations (Figure 2a), as well as high tensile stresses on the surface of {100} lateral planes that are situated at 45° angles from the preferentially expanded {110} planes, explaining cracking initiation at these locations.

We simulated the morphological evolution of coated nanopillars with various h and A coating parameters. As the adopted chemomechanical model has no intrinsic length scale, model predictions depend on the h/A ratio only. A remarkable effect of the coating is to buffer the volume expansion through nonuniform deformation of the coating, effectively reducing the overall anisotropy of the structure (Figure 3a; see also Figure S3b). The buffering effect increases with the relative coating thickness. The model also predicts the largest hoop stress levels and plastic strain accumulation on the coating surface along the ⟨110⟩ directions (Figure 3b and c for the case h/A = 1/6; see also Supporting Information Figure S7), as a result of the faster front velocity. Qualitatively similar trends are found for h/A = 1/4, 1/3, 1/2. These trends are consistent with the reduced anisotropy observed experimentally when the coating thickness increases. It also explains the initiation of cracking on the surface of {110} lateral planes in structures with a relatively thin coating (Si_{480}@Ni_{40} or h/A = 1/6, Figure 2b). However, these predictions are not sufficient to explain the random location of cracks for relatively thick coatings, namely, the cases Si_{480}@Ni_{120} (h/A = 1/2), Si_{330}@Ni_{90} ($h/A \approx$ 1/2), Si_{330}@Ni_{40} ($h/A \approx$ 1/4), and Si_{170}@Ni_{40} ($h/A \approx$ 1/2) (see also Figure 2c). As a matter of fact, the mechanical constraint induced by the Ni coating is expected to have an impact on the reaction kinetics, as discussed below.

Another important argument that could explain the transition from anisotropic to isotropic swelling and fracture behavior is based on kinetic considerations. It has been shown in several studies that the high compressive stresses that develop at the lithiation front could slow down the chemical reaction.[43−45] In a recent study, Zhao *et al*. identified the driving force for reaction as the net change in free energy resulting from the conversion of one Li atom and 1/x Si atoms into lithiated silicon:[43]

$$\Delta G = \Delta G_r - e\Phi + \frac{1}{x}(\sigma_m^{Si}\Omega^{Si} - \sigma_m^{Li_xSi}\Omega^{Li_xSi}) \quad (1)$$

where ΔG_r is the chemical driving force in the absence of stress and externally applied voltage, $-e\Phi$ is the contribution from the applied voltage, and the last term represents the change in free energy of the system by mechanical work at the front. Here, σ_m^{Si} and $\sigma_m^{Li_xSi}$ are the mean stress at the reaction front respectively on the c-Si core and lithiated shell side, while Ω^{Si} and Ω^{Li_xSi} correspond to the volumes of the molecular units. Expression 1 indicates that the volume-weighted pressure difference across the reaction front can

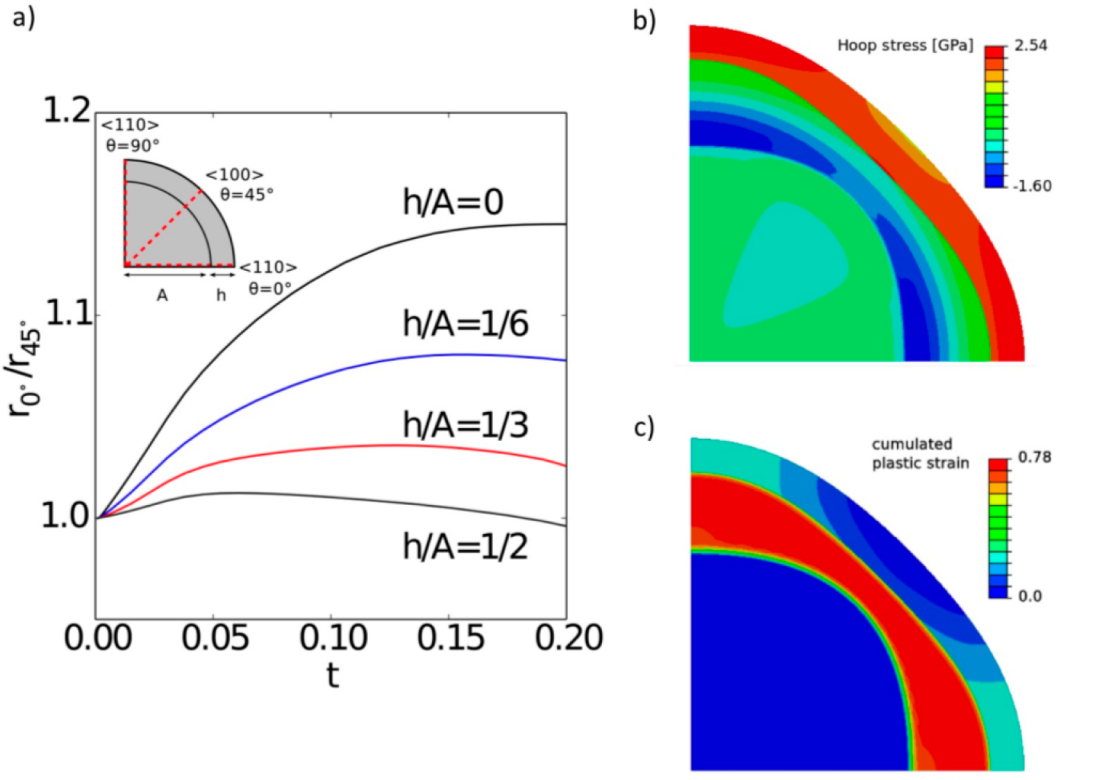

Figure 3. Buffering action of the shell. (a) Numerical simulations indicate that the coating reduces the overall anisotropic expansion of the nanostructure by buffering the swelling strain. The anisotropy is measured by the predicted ratio of current outer radii at 0° and 45° ($r_{0°}/r_{45°}$) for normalized lithiation time ($0 \leq t \leq 0.2$). Contours of (b) hoop stress and (c) cumulated plastic strain for h/A = 1/6 (representative of $Si_{480}@Ni_{40}$). The highest tensile hoop stresses in the Ni shell are found along the ⟨110⟩ directions. Qualitatively similar contour plots are obtained in the simulations with h/A = 1/4, 1/3, and 1/2.

contribute positively or negatively to the reaction kinetics.

Numerically predicted hydrostatic stress profiles are shown in Figure 4 for different h/A ratios together with the corresponding normalized concentration profile, in the ⟨110⟩ and ⟨100⟩ directions. Because the concentration admits a smooth transition between 0 (unlithiated) and 1 (fully lithiated) in the model, eq 1 cannot be strictly applied. However, it is clear from Figure 4a that the h/A ratio significantly impacts the hydrostatic stress levels near the front and delays the reaction in ⟨110⟩ directions. In contrast, Figure 4b indicates that the delayed contribution of the stress has a lower impact for the directions ⟨100⟩. This effect plays a role in all configurations, but is less important for small h/A ratio. Overall, the numerical results suggest that the presence of the coating increases the hydrostatic pressure at the front, which presumably slows down the lithiation kinetics as a whole and, furthermore, reduces the swelling anisotropy.

On the basis of these considerations, it is likely that the mechanical constraint induced by the thick coating ($Si_{480}@Ni_{120}$, h/A = 1/2) strongly limits the extent of lithiation, as well as the swelling anisotropy, leading to more isotropic stress distribution and a single randomly located fracture site. A recent report detailing broken lithiation symmetry through external mechanical action further corroborates our findings.[46] Faster lithiation of Ge nanowires was found on the side under tension, whereas the reaction kinetics slowed down in compressive regions. As can be seen in Figure 4c, when the ratio of the front velocities along the ⟨110⟩ and ⟨100⟩ directions is close to 1, the hoop stress distribution in the Ni shell is almost uniform. Fracture is then dominated by defects existing in the thick shell (*i.e.*, roughness and grain boundary grooving), rather than by stress or plastic strain concentration. The defect-dominated fracture hypothesis is also supported by the additional experiments (see Supporting Information, Figure S8).

The mechanical constraint of the thick shell acts even after the initiation of a crack. Indeed, the $Si_{480}@Ni_{120}$ nanopillars display different degrees of swelling (and hence lithiation), as well as different crack extensions (Figure 2c) despite forced lithiation during prolonged times (by holding the voltage at 10 mV *vs* Li/Li^+ for more than 24 h). Even after the onset of fracture, lithiation is sometimes unable to proceed. This is surprising, as one would expect the unzipping of the core−shell structure to relax stresses, enabling the lithiation to proceed faster through the fracture region (Supporting Information, Figure S9). This indicates that the undamaged portion of the Ni layer is able to maintain its strong mechanical constraint, preventing

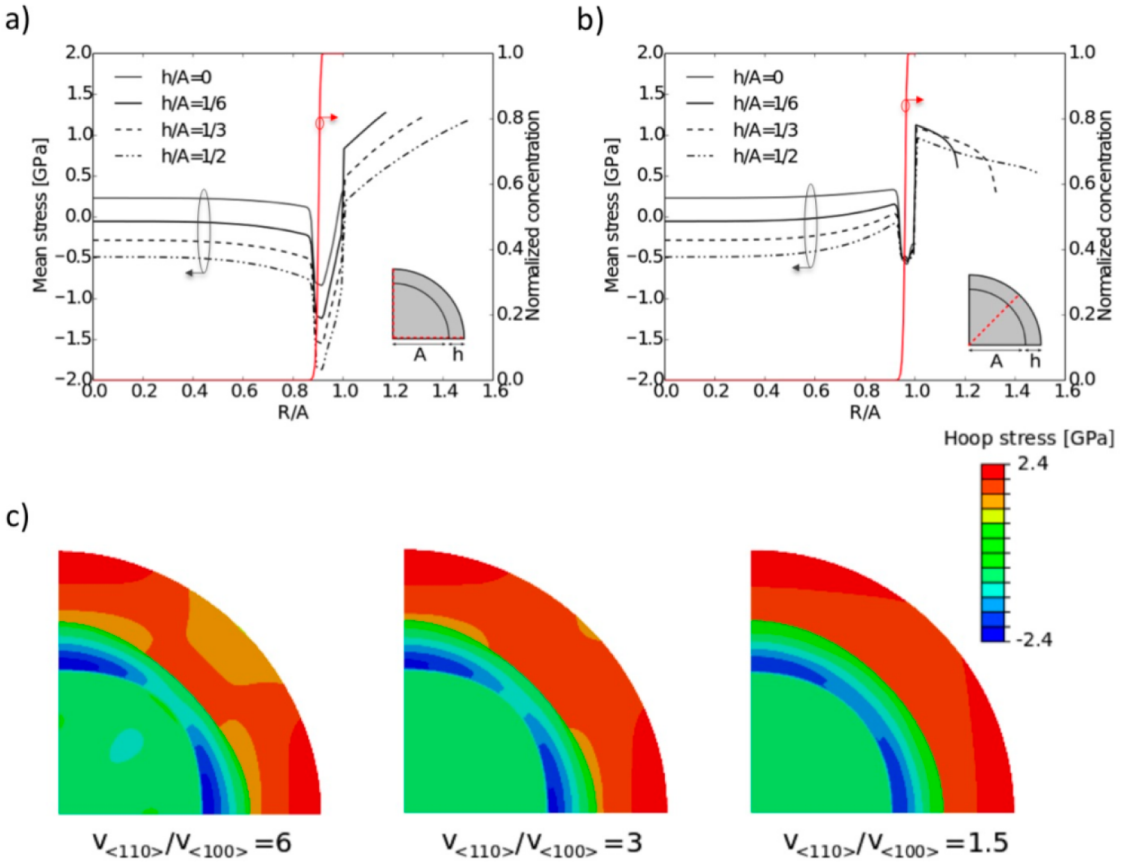

Figure 4. Stress effect on lithiation kinetics. The mean stress profiles along the (a) ⟨110⟩ and (b) ⟨100⟩ directions for different *h*/*A* ratios at the beginning of lithiation. Here *R* is the radial coordinate in the undeformed configuration. The corresponding normalized concentration profile is also represented on the right-hand-side ordinate-axis. Thicker coatings considerably increase the magnitude of the compressive stress in the ⟨110⟩ directions and slow down the reaction in this direction, hence reducing the anisotropy, as well as the global reaction kinetics. (c) Contours of hoop stress in the Ni shell for different ratios of the front velocities in the ⟨110⟩ ($v_{\langle 110\rangle}$) and ⟨100⟩ ($v_{\langle 100\rangle}$) directions. When this ratio is close to 1 (for instance, due to stress effect on the lithiation kinetics), the tensile hoop stress is more homogeneous. Such a scenario explains the random fracture pattern experimentally observed in nanopillars with a thick coating.

further lithiation (or core expansion). Finally, some of the nanopillars in the Si_{480}@Ni_{120} configuration did not experience any swelling or fracture, indicating that the coating may completely impede the reaction in some cases.

DISCUSSION

The adopted model provides insight into the experimental trends, although we could not determine the actual ratio of the reaction front velocities in the ⟨110⟩ and ⟨100⟩ directions in the considered configurations. This ratio is affected by the local stress and thus evolves in time; *in situ* monitoring could reveal additional features of lithiation kinetics in coated structures.[47] According to our model, the same trends are expected for a given *h*/*A* ratio, independently of the radius *A*. However, some discrepancies are found when comparing the behavior of small-diameter nanowires (2*A* = 330 nm) and larger diameter (2*A* = 480 nm). Relying solely on the *h*/*A* ratio, anisotropic swelling and fracture pattern would be expected for the $Si_{330}Ni_{40}$ nanopillars (*h*/*A* = 1/4), as both the $Si_{480}Ni_{40}$ (*h*/*A* = 1/6) and $Si_{480}Ni_{80}$ (*h*/*A* = 1/3) display anisotropic behavior. In contrast, a preferentially isotropic behavior was observed for the $Si_{330}Ni_{40}$ configuration (although specificity along {110} planes could be detected as well; see Figure S3). Additional size-dependent effects play a subtle role. Here, the isotropic behavior of the $Si_{330}Ni_{40}$ nanopillars is reminiscent of the reduced anisotropy observed in uncoated pillars of small diameters (see Supporting Information, Figures S3 and S4) also reported by other groups. Experimental observations showed that below a critical size of approximately 300 nm the anisotropic expansion is less pronounced and fracture can be avoided.[34,40] Hence, the radius of the Si core (*i.e.*, its curvature) affects the lithiation kinetics, irrespective of the presence of a coating layer. To the best of our knowledge, the physical origin of this size effect has not been elucidated yet. Note finally that the size effect can also result from the complex thickness dependence of the strength and ductility of the Ni film, which is out of the scope of this investigation.[48]

For *h*/*A* values close to 1/3, the lithiated structures display a peculiar cracking pattern. The volume

expansion of the core leads to the unzipping of the shell, and the cracking (and the lithiation) further progresses in the radial direction with significant shell deformation, finally leading to a fully open frame (Figure 2c; Supporting Information, Figures S3, S4, and S9). The main difference observed for the $Si_{480}@Ni_{120}$ configuration is that the Ni shell deforms less, preserving the initial circular shape. This suggests a larger structural stiffness of the thicker Ni coatings.

The fracture pattern that develops during the first lithiation will most probably have a first-order impact on the cyclic performance of the electrode. In particular, thick coating structures display isotropic expansion as well as a single crack that unzips the shell and propagates into the core. Most of these structures, upon extended lithiation (*i.e.*, full unzipping and longitudinal opening), lead to a configuration resembling a Si thin film on a Ni substrate (Figure 2c). Note that, although the metal substrate maintains its curvature for the thicker coatings, structures with isotropic cracks show flattening to a certain extent (as exemplified in Figures S3, S4, and S9). The thin-film configuration is known to sustain repeatable cycling due to unconstrained, reversible volume changes.[3,49] Such a configuration also minimizes the exposed silicon surface in contact with the electrolyte (as compared to a multicracked configuration). These observations could be relevant to understand literature results reporting enhanced cycling of coated nanowires.

Our findings further suggest a route for the design of alternative nanostructures through proper control of the fracture pattern during initial lithiation. In the present work we were not able to perform several Li insertion and extraction cycles due to the pulverization of the underlying silicon substrate during the first lithiation (Supporting Information, Figure S10). Nonetheless, we expect structures exhibiting isotropic swelling and cracking ($Si_{480}@Ni_{120}$, $Si_{330}@Ni_{40}$, $Si_{330}@Ni_{90}$, and $Si_{170}@Ni_{40}$) to show better cycling performances. Additional work is called for to experimentally ascertain this behavior. Although the initial lithiation is clearly impeded by the coating, engineered structures with defects introduced on purpose could be used to accelerate the initial lithiation (Supporting Information, Figure S8).

CONCLUSION

In conclusion, we addressed nickel-coated ⟨100⟩ silicon nanopillars as a model system to study the deformation and fracture of core−shell nanostructured anodes during the initial Li insertion cycle. Coated structures display different swelling and cracking regimes depending primarily on the coating thickness to pillar diameter ratio. For low ratios, the swelling and cracking are anisotropic, although with different fracture sites compared to uncoated nanopillars. The swelling behavior progressively becomes isotropic when the ratio increases, which is attributed to the large stress-induced slowing down of the reaction kinetics. This effect is more pronounced in the ⟨110⟩ directions. In addition, the intrinsic values of the pillar diameter and coating thickness are likely to play a role. A more detailed chemomechanical model is needed to investigate the role of intrinsic lengths, as well as to ascertain the real-time lithiation dynamics.

Although we restricted our analysis to the initial lithiation, we believe that the specific deformation and fracture patterns that develop at this stage will crucially impact the anode performance during subsequent cycles. The insight provided here further suggests a route for the design of coated anodes through the proper control of the deformation and fracture pattern. A deeper fundamental understanding of the initial lithiation, in addition to cyclic lithiation studies, is required in view of developing enhanced electrodes based on coated nanostructures.

METHODS

Silicon Nanopillar (SiNP) Fabrication. SiNPs were prepared by metal-assisted chemical etching as previously described.[10] Briefly, polystyrene (PS) colloidal particles with 170, 330, and 480 nm nominal diameters (Microparticles Gmbh) were dispersed on Si chips (p-type ⟨100⟩, resistivity of 10−25 Ωcm). Next, 1 nm Ti and 30 nm Au were deposited on the Si substrate by physical vapor deposition. The lift-off of the PS spheres was done with adhesive tape followed by rinsing in CH_2Cl_2. The metal-assisted chemical etching of Si was done in an aqueous solution containing 0.2 M H_2O_2 and 4.8 M HF at room temperature and under continuous agitation. After etching, the samples were rinsed with deionized water and allowed to dry in air. The Au mask was dissolved by submerging the samples in HNO_3/HCl (1:3 by volume). Subsequently, the samples were rinsed in deionized water and allowed to dry in air.

Electroless Conformal Ni Coating. The electroless protocol was adapted from the literature.[50,51] Briefly, a Ni electroless deposition bath was prepared by dissolving 2 g of nickel sulfate hexahydrate (Sigma-Aldrich), 1 g of sodium citrate (Sigma-Aldrich) complexant, 0.5 g of lactic acid (Sigma-Aldrich) as buffer, and 0.1 g of dimethylamine borane (Acros Organics) in 50 mL of deionized water. The pH was adjusted to ∼7 with ammonium hydroxide. The electroless deposition of Ni was carried out at room temperature or in a thermostated bath (40−60 °C) under continuous agitation. The onset of the deposition was visually identified by the appearance and evolution of gas bubbles at the surface of the samples. After this point, the soaking time varied from 10 to 120 min depending on the target coating thickness. After the deposition, the sample was rinsed in water and methanol and allowed to dry in air.

***Ex Situ* Experimental Protocol.** Swagelok-type half-cells were assembled inside an Ar-filled glovebox (MBraun) by stacking either pristine SiNPs or Ni-coated SiNPs on the Si substrate, a separator (Celgrad) soaked in electrolyte (1 M $LiPF_6$ in ethylenecarbonate/diethyl carbonate, 1:1 by volume, Novolyte), and Li-metal foil (Sigma-Aldrich). A slow voltammetry scan (0.1 mV/s) was performed from the open-circuit voltage of the cell down to 10 mV *vs* Li/Li^+ using an Arbin BT2043 battery analyzer. The potential was held for at least 6 h for full lithiation

of the uncoated pillars. This result was checked by selective methanol washing of the lithiated silicon phase, which revealed no sign of subsisting c-Si (see for comparison Figure S9c, displaying the crystalline Si core upon a short lithiation time of a pristine Si pillar). For metal-coated structures, the potential was held for much longer periods, ranging from 12 to 48 h. After lithiation, the cell was disassembled in the glovebox and the sample rinsed in acetonitrile (Sigma-Aldrich) to remove any surface residues. The lithiated sample was then placed in an Ar-filled container to have a minimal exposure to the environmental air and then transferred for inspection by SEM.

Conflict of Interest: The authors declare no competing financial interest.

Acknowledgment. L.B., S.M., and A.V. are mandated by the National Fund for Scientific Research (F.R.S.—FNRS, Belgium). We thank J. Rolland and J.-P. Bourgeois for experimental assistance and TEM characterization. L.B. thanks I. Ryu, M. Pharr, and K. J. Zhao for useful discussions regarding the model implementation. A.V., J.F.G., and S.M. are grateful to the Walloon Region for financial support in the frame of the BATWAL "Programme d'Excellence" and "ERable" Programme. This research connects to the ARC project entitled "TINTIN" (No. 09/14-023) sponsored by the Communauté Française de Belgique and to the F.R.S.—FNRS project entitled "ECOSTOFLEX".

Supporting Information Available: Supporting figures of the morphology of Si—Ni nanostructures, fracture location statistics for $Si_{480}@Ni_{40}$ and $Si_{480}@Ni_{80}$ nanowires, lithiation dynamics and fracture location statistics for core—shell nanowires with 330 and 170 nm diameter Si core, numerically predicted lithiation profiles in uncoated nanopillars as well as contour plots of the normalized Li concentration for pristine and Ni-coated ($h/A = 1/6$ and 1/2) nanopillars, mean stress profiles and contour plots of hoop stress in uncoated nanopillars, stress profiles at $\theta = 0°$ and 45° in Ni-coated nanopillars for $h/A = 1/6$, asymmetric Ni coating for controlling the cracking site, the morphological evolution of Si nanopillars during lithiation, as well as the lithiation-induced swelling of the underlying Si substrate. This material is available free of charge *via* the Internet at http://pubs.acs.org.

REFERENCES AND NOTES

1. Armand, M.; Tarascon, J.-M. Building Better Batteries. *Nature* **2008**, *451*, 652–657.
2. Obrovac, M. N.; Christensen, L. Structural Changes in Silicon Anodes during Lithium Insertion/Extraction. *Electrochem. Solid-State Lett.* **2004**, *7*, A93–A96.
3. Beaulieu, L. Y.; Eberman, K. W.; Turner, R. L.; Krause, L. J.; Dahn, J. R. Colossal Reversible Volume Changes in Lithium Alloys. *Electrochem. Solid-State Lett.* **2001**, *4*, A137–A140.
4. Nadimpalli, S. P. V.; Sethuraman, V. A.; Dalavi, S.; Lucht, B.; Chon, M. J.; Shenoy, V. B.; Guduru, P. R. Quantifying Capacity Loss Due to Solid-Electrolyte-Interphase Layer Formation on Silicon Negative Electrodes in Lithium-Ion Batteries. *J. Power Sources* **2012**, *215*, 145–151.
5. Gao, B.; Sinha, S.; Fleming, L.; Zhou, O. Alloy Formation in Nanostructured Silicon. *Adv. Mater.* **2001**, *13*, 816–819.
6. Chan, C. K.; Peng, H.; Liu, G.; McIlwrath, K.; Zhang, X. F.; Huggins, R. A.; Cui, Y. High-Performance Lithium Battery Anodes Using Silicon Nanowires. *Nat. Nanotechnol.* **2008**, *3*, 31–35.
7. Cui, L.-F.; Ruffo, R.; Chan, C. K.; Peng, H.; Cui, Y. Crystalline-Amorphous Core—Shell Silicon Nanowires for High Capacity and High Current Battery Electrodes. *Nano Lett.* **2009**, *9*, 491–495.
8. Magasinski, A.; Dixon, P.; Hertzberg, B.; Kvit, A.; Ayala, J.; Yushin, G. High-Performance Lithium-Ion Anodes Using a Hierarchical Bottom-up Approach. *Nat. Mater.* **2010**, *9*, 353–358.
9. Karki, K.; Zhu, Y.; Liu, Y.; Sun, C.-F.; Hu, L.; Wang, Y.; Wang, C.; Cumings, J. Hoop-Strong Nanotubes for Battery Electrodes. *ACS Nano* **2013**, *7*, 8295–8302.
10. Vlad, A.; Reddy, A. L. M.; Ajayan, A.; Singh, N.; Gohy, J.-F.; Melinte, S.; Ajayan, P. M. Roll Up Nanowire Battery from Silicon Chips. *Proc. Natl. Acad. Sci. U.S.A.* **2012**, *109*, 15168–15173.
11. Kovalenko, I.; Zdyrko, B.; Magasinski, A.; Hertzberg, B.; Milicev, Z.; Burtovyy, R.; Luzinov, I.; Yushin, G. A Major Constituent of Brown Algae for Use in High-Capacity Li-Ion Batteries. *Science* **2011**, *334*, 75–79.
12. Liu, G.; Xun, S.; Vukmirovic, N.; Song, X.; Olalde-Velasco, P.; Zheng, H.; Battaglia, V. S.; Wang, L.; Yang, W. Polymers with Tailored Electronic Structure for High Capacity Lithium Battery Electrodes. *Adv. Mater.* **2011**, *23*, 4679–4683.
13. Dalavi, S.; Guduru, P.; Lucht, B. L. Performance Enhancing Electrolyte Additives for Lithium Ion Batteries with Silicon Anodes. *J. Electrochem. Soc.* **2012**, *159*, A642–A646.
14. Memarzadeh, E. L.; Kalisvaart, W. P.; Kohandehghan, A.; Zahiri, B.; Holtab, C. M. B.; Mitlin, D. Silicon Nanowire Core Aluminum Shell Coaxial Nanocomposites for Lithium Ion Battery Anodes Grown with and without a TiN Interlayer. *J. Mater. Chem.* **2012**, *22*, 6655–6668.
15. Sethuraman, V. A.; Kowolik, K.; Srinivasan, V. Increased Cycling Efficiency and Rate Capability of Copper-Coated Silicon Anodes in Lithium-Ion Batteries. *J. Power Sources* **2011**, *196*, 393–398.
16. Usui, H.; Uchida, N.; Sakaguchi, H. Influence of Order in Stepwise Electroless Deposition on Anode Properties of Thick-Film Electrodes Consisting of Si Particles Coated with Ni and Cu. *J. Power Sources* **2011**, *196*, 10244–10248.
17. Wu, H.; Chan, G.; Choi, J. W.; Ryu, I.; Yao, Y.; McDowell, M. T.; Lee, S. W.; Jackson, A.; Yang, Y.; Hu, L.; *et al.* Stable Cycling of Double-Walled Silicon Nanotube Battery Anodes Through Solid-Electrolyte Interphase Control. *Nat. Nanotechnol.* **2012**, *7*, 310–315.
18. Li, J.; Xiao, X.; Cheng, Y.-T.; Verbrugge, M. W. Atomic Layered Coating Enabling Ultrafast Surface Kinetics at Silicon Electrodes in Lithium Ion Batteries. *J. Phys. Chem. Lett.* **2013**, *4*, 3387–3391.
19. Kohandehghan, A.; Kalisvaart, P.; Cui, K.; Kupsta, M.; Memarzadeh, E.; Mitlin, D. Silicon Nanowire Lithium-Ion Battery Anodes with ALD Deposited TiN Coatings Demonstrate a Major Improvement in Cycling Performance. *J. Mater. Chem.* **2013**, *1*, 12850–12861.
20. McDowell, M. T.; Woo Lee, S.; Wang, C.; Cui, Y. The Effect of Metallic Coatings and Crystallinity on the Volume Expansion of Silicon During Electrochemical Lithiation/Delithiation. *Nano Energy* **2012**, *1*, 401–410.
21. Zhang, L. Q.; Liu, X. H.; Liu, Y.; Huang, S.; Zhu, T.; Gui, L.; Mao, S. X.; Ye, Z. Z.; Wang, C. M.; Sullivan, J. P.; *et al.* Controlling the Lithiation-Induced Strain and Charging Rate in Nanowire Electrodes by Coating. *ACS Nano* **2011**, *5*, 4800–4809.
22. Murugesan, S.; Harris, J. T.; Korgel, B. A.; Stevenson, K. J. Copper-Coated Amorphous Silicon Particles as an Anode Material for Lithium-Ion Batteries. *Chem. Mater.* **2012**, *24*, 1306–1315.
23. Lee, S.; Ha, J.; Cheng, H.; Lee, J. W.; Jang, T. S.; Jung, Y.-G.; Huang, Y.; Rogers, J. A.; Paik, U. Surface-Coverage-Dependent Cycle Stability of Core-Shell Nanostructured Electrodes for Use in Lithium Ion Batteries. *Adv. Energy Mater.* **2014**, *4*, 1300472.
24. Karki, K.; Epstein, E.; Cho, J.-H.; Jia, Z.; Li, T.; Picraux, S. T.; Wang, C.; Cumings, J. Lithium-Assisted Electrochemical Welding in Silicon Nanowire Battery Electrodes. *Nano Lett.* **2012**, *12*, 1392–1397.
25. Hovington, P.; Dontigny, M.; Guerfi, A.; Trottier, J.; Lagacé, M.; Mauger, A.; Julien, C. M.; Zaghib, K. *In Situ* Scanning Electron Microscope Study and Microstructural Evolution of Nano Silicon Anode for High Energy Li-Ion Batteries. *J. Power Sources* **2014**, *248*, 457–464.
26. Gu, M.; Li, Y.; Li, X.; Hu, S.; Zhang, X.; Xu, W.; Thevuthasan, S.; Baer, D. R.; Zhang, J.-G.; Liu, J.; *et al.* *In Situ* TEM Study of Lithiation Behavior of Silicon Nanoparticles Attached to and Embedded in a Carbon Matrix. *ACS Nano* **2012**, *6*, 8439–8447.
27. Liu, Y.; Zheng, H.; Liu, X. H.; Huang, S.; Zhu, T.; Wang, J.; Kushima, A.; Hudak, N. S.; Huang, X.; Zhang, S.; *et al.*

Lithiation-Induced Embrittlement of Multiwalled Carbon Nanotubes. *ACS Nano* **2011**, *5*, 7245–7253.
28. Hertzberg, B.; Alexeev, A.; Yushin, G. Deformations in Si−Li Anodes upon Electrochemical Alloying in Nano-Confined Space. *J. Am. Chem. Soc.* **2010**, *132*, 8548–8549.
29. Zhao, K.; Pharr, M.; Hartle, L.; Vlassak, J. J.; Suo, Z. Fracture and Debonding in Lithium-Ion Batteries with Electrodes of Hollow Core−Shell Nanostructures. *J. Power Sources* **2012**, *218*, 6–14.
30. Hassoun, J.; Agostini, M.; Latini, A.; Panero, S.; Sun, Y.-K.; Scrosati, B. Nickel-Layer Protected, Carbon-Coated Sulfur Electrode for Lithium Battery. *J. Electrochem. Soc.* **2012**, *159*, A390–A395.
31. Usui, H.; Shibata, M.; Nakai, K.; Sakaguchi, H. Anode Properties of Thick-Film Electrodes Prepared by Gas Deposition of Ni-Coated Si Particles. *J. Power Sources* **2011**, *196*, 2143–2148.
32. Yu, P.; Ritter, J. A.; White, R. E.; Popov, B. N. Ni-Composite Microencapsulated Graphite as the Negative Electrode in Lithium-Ion Batteries II: Electrochemical Impedance and Self-Discharge Studies. *J. Electrochem. Soc.* **2000**, *147*, 2081–2085.
33. Lee, S. W.; McDowell, M. T.; Choi, J. W.; Cui, Y. Anomalous Shape Changes of Silicon Nanopillars by Electrochemical Lithiation. *Nano Lett.* **2011**, *11*, 3034–3039.
34. Lee, S. W.; McDowell, M. T.; Berla, L. A.; Nix, W. D.; Cui, Y. Fracture of Crystalline Silicon Nanopillars During Electrochemical Lithium Insertion. *Proc. Natl. Acad. Sci. U.S.A.* **2012**, *109*, 4080–4085.
35. Liu, X. H.; Zheng, H.; Zhong, L.; Huang, S.; Karki, K.; Zhang, L. Q.; Liu, Y.; Kushima, A.; Liang, W. T.; Wang, J. W.; *et al*. Anisotropic Swelling and Fracture of Silicon Nanowires during Lithiation. *Nano Lett.* **2011**, *11*, 3312–3318.
36. Baggetto, L.; Danilov, D.; Notten, P. H. L. Honeycomb-Structured Silicon: Remarkable Morphological Changes Induced by Electrochemical (De)Lithiation. *Adv. Mater.* **2011**, *23*, 1563–1566.
37. Pharr, M.; Zhao, K.; Wang, X.; Suo, Z.; Vlassak, J. J. Kinetics of Initial Lithiation of Crystalline Silicon Electrodes of Lithium-Ion Batteries. *Nano Lett.* **2012**, *12*, 5039–5047.
38. Yang, H.; Huang, S.; Huang, X.; Fan, F.; Liang, W.; Liu, X. H.; Chen, L.-Q.; Huang, J. Y.; Li, J.; Zhu, T.; *et al*. Orientation-Dependent Interfacial Mobility Governs the Anisotropic Swelling in Lithiated Silicon Nanowires. *Nano Lett.* **2012**, *12*, 1953–1958.
39. Liu, X. H.; Wang, J. W.; Huang, S.; Fan, F.; Huang, X.; Liu, Y.; Krylyuk, S.; Yoo, J.; Dayeh, S. A.; Davydov, A. V.; *et al*. *In Situ* Atomic-Scale Imaging of Electrochemical Lithiation in Silicon. *Nat. Nanotechnol.* **2012**, *7*, 749–756.
40. Ryu, I.; Lee, S. W.; Gao, H.; Cui, Y.; Nix, W. D. Microscopic Model for Fracture of Crystalline Si Nanopillars during Lithiation. *J. Power Sources* **2014**, *255*, 274–282.
41. Liu, X. H.; Zhong, L.; Huang, S.; Mao, S. X.; Zhu, T.; Huang, J. Y. Size-Dependent Fracture of Silicon Nanoparticles during Lithiation. *ACS Nano* **2012**, *6*, 1522–1531.
42. Chon, M. J.; Sethuraman, V. A.; McCormick, A.; Srinivasan, V.; Guduru, P. R. Real-Time Measurement of Stress and Damage Evolution during Initial Lithiation of Crystalline Silicon. *Phys. Rev. Lett.* **2011**, *107*, 045503.
43. Zhao, K.; Pharr, M.; Wan, Q.; Wang, W. L.; Kaxiras, E.; Vlassak, J. J.; Suo, Z. Concurrent Reaction and Plasticity during Initial Lithiation of Crystalline Silicon in Lithium-Ion Batteries. *J. Electrochem. Soc.* **2012**, *159*, A238–A243.
44. McDowell, M. T.; Ryu, I.; Lee, S. W.; Wang, C.; Nix, W. D.; Cui, Y. Studying the Kinetics of Crystalline Silicon Nanoparticle Lithiation with *in Situ* Transmission Electron Microscopy. *Adv. Mater.* **2012**, *24*, 6034–6041.
45. Liu, X. H.; Fan, F.; Yang, H.; Zhang, S.; Huang, J. Y.; Zhu, T. Self-Limiting Lithiation in Silicon Nanowires. *ACS Nano* **2013**, *7*, 1495–1503.
46. Gu, M.; Yang, H.; Perea, D. E.; Zhang, J.-G.; Zhang, S.; Wang, C. Bending-Induced Symmetry Breaking of Lithiation in Germanium Nanowires. *Nano Lett.* **2014**, *14*, 4622–4627.
47. Liu, X. H.; Liu, Y.; Kushima, A.; Zhang, S.; Zhu, T.; Li, J.; Huang, J. Y. *In Situ* TEM Experiments of Electrochemical Lithiation and Delithiation of Individual Nanostructures. *Adv. Energy Mater.* **2012**, *2*, 722–741.
48. Pardoen, T. Size and Rate Dependent Necking in Thin Metallic Films. *J. Mech. Phys. Solids* **2014**, *62*, 81–98.
49. Phan, V. P.; Pecquenard, B.; Le Cras, F. High-Performance All-Solid-State Cells Fabricated with Silicon Electrodes. *Adv. Funct. Mater.* **2012**, *22*, 2580–2584.
50. Lancaster, J. R.; Jehani, J.; Carroll, G. T.; Chen, Y.; Turro, N. J.; Koberstein, J. T. Toward a Universal Method To Pattern Metals on a Polymer. *Chem. Mater.* **2008**, *20*, 6583–6585.
51. Tan, Y.; Gu, J.; Zang, X.; Xu, W.; Shi, K.; Xu, L.; Zhang, D. Versatile Fabrication of Intact Three-Dimensional Metallic Butterfly Wing Scales with Hierarchical Sub-micrometer Structures. *Angew. Chem.* **2011**, *123*, 8457–8461.